NUMERICAL ANALYSIS OF THE UNSTEADY FLOW ABOVE A SLENDER DELTA WING AT LARGE ANGLES OF ATTACK

J. Müller , D. Hummel
Institute of Fluid Mechanics, Technical University Braunschweig, Germany

Abstract

The unsteady, bursted vortical flow above the fixed VFE delta wing at large angles of attack $\alpha \geq 18°$ was analyzed by time-accurate Euler and Navier-Stokes calculations. For an inviscid Euler code the situation within the primary vortex core is dominated by numerical dissipation. The same is true for a Navier-Stokes code using the algebraic Baldwin-Lomax turbulence model, which only provides additional turbulent eddy viscosity within the boundary layer near the wall. Therefore, both methods have to be calibrated e.g. by an experimentally proved breakdown position. On the other hand, the two-equations k-ω turbulence model of Wilcox is able to provide sufficient turbulent eddy viscosity within the primary vortex core. Such a method becomes independent from the artificial numerical dissipation $k^{(4)}$ and the grid resolution.

The time-accurate Euler calculations were calibrated at $\alpha = 18°$. Such an adapted Euler code is able to predict the breakdown positions and the frequencies of the breakdown process correctly for almost the whole angle of attack range. The influence of the secondary vortex on the breakdown process of the primary vortex is limited to small angles of attack $\alpha \leq 23°$ and leads for a calibrated Euler calculation to a further downstream located breakdown position and to higher dominating frequencies compared to Navier-Stokes results. For higher angles of attack the differences diminish. Finally, the deadwater-type flow at very high angles of attack $\alpha \geq 43°$ is predicted identically by both numerical methods.

1 Introduction

The correct prediction of the maximum lift of a delta wing is of great technical interest for combat aircrafts maneouvering at large angles of attack. The flow past a sharp edged delta wing differs significantly from the flow past a conventional wing. Even at small angles of attack the flow separates at the leading edges, forming two spiral primary vortices. Each of these vortices causes a second boundary-layer separation beneath them, leading to an associated small counter-rotating secondary vortex. The main effect of the secondary vortex is to displace the primary vortex upwards and inwards compared with the inviscid case. At higher angles of attack the primary vortices are bursting, which means the vortex axes are experiencing a spiral mo-

tion with respect to space and a rotation with respect to time. This phenomenon of vortex breakdown results in a decline of the lift curve and causes the flow above a fixed delta wing to become *unsteady*. With increasing angle of attack the breakdown position moves upstream and the produced lift reaches its maximum value. If the breakdown position reaches the apex of the wing, the bursted vortical flow suddenly disappears and a deadwater-type flow establishes.

The complex vortical flow above a sharp-edged delta wing, especially the unsteady phenomenon of vortex breakdown, has been investigated in the wind-tunnel for many years (see e.g. [1] - [5]). During the last two decades computational fluid dynamics has become a powerful tool to provide new insights into the unsteady delta wing flow [6] - [8]. Nevertheless, most of the numerical investigations have been carried out by non time-accurate flow solvers, see e.g. J. Longo [9] and D. Strohmeyer et al. [10], DLR Braunschweig[*]. Since the flow above a delta wing at high angles of attack becomes unsteady only *time-accurate* methods are able to predict the breakdown position and the dominating frequencies of the breakdown process correctly. These methods also supply the correct amount of maximum lift.

At the Institute of Fluid Mechanics of Technical University Braunschweig time-accurate calculations have been carried out for the sharp-edged delta wing of the "International Vortex Flow Experiment, VFE" (see G. Drougge [11]). For this configuration defined in 1986 a large amount of computational and experimental data exists. It consists of a $65°$ swept and cropped delta wing with an aspect ratio of $A = 1.38$ and a symmetrical airfoil (Fig. 1). Since the first computations by J. Müller and D. Hummel [12], [13] were mainly performed by a time-accurate but inviscid Euler code, the present paper focusses on the corresponding time-accurate viscous Navier-Stokes calculations. Even at small angles of attack, the missing secondary vortices in an Euler calculation cause substantially different pressure distributions and force coefficients in comparison with Navier-Stokes results [13]. At high angles of attack, it remains to analyse the influence of the secondary vortex on the breakdown process of the primary vortex.

---

[*]Deutsches Zentrum für Luft- und Raumfahrt

2 Notations

A	Aspect ratio, $A = b^2/S$
b	Wing span
c	Root chord
$c_1(y)$	Local chord
c_t	Tip chord
c_μ	Reference chord, $c_\mu = \frac{1}{S}\int_s^s c_1^2(y)dy$
C_L, C_D, C_m	Lift, drag and pitching moment coefficients, based on q_∞, S, c_μ, reference point: N_{25}, nose-up positive
C_p	Static pressure coefficient, $C_p = (p - p_\infty)/q_\infty$
d	Root thickness
i, j, k	Curvelinear grid coordinates, see Fig. 2
$k^{(4)}$	Fourth order artificial damping coefficient
n	number of time-steps
N_{25}	Geometric neutral point
M_∞	Free stream Mach number
p	Static pressure
p_t	Total pressure
q_∞	Dynamic pressure
Re_∞	Free stream Reynolds number, $Re_\infty = U_\infty c/\nu$
s	Half wing span, $s = b/2$
$s_1(x)$	Local half span
S	Wing area
t	Time
t^*	Non-dimensional time, $t^* = t \cdot U_\infty/c$
Δt^*	Non-dimensional time step, $\Delta t^* = \Delta t \cdot U_\infty/c$
T^*	Non-dimensional period, $T^* = T \cdot U_\infty/c$
u_a	Axial velocity
U_∞	Free stream velocity
x, y, z	Rectangular wing fixed coordinates, see Fig. 1
α	Angle of attack
ϑ	Nose angle, see Fig. 1
ν	Kinematic viscosity
φ	Leading edge sweep angle
ω^*	Reduced radian frequency, $\omega^* = 2\pi/T^*$
ω_1^*	Highest dominating frequency of the azimuthal mode
ω_{1e}^*	Highest dominating frequency according to the experimental correlation of Breitsamter [22]

Sub- and superscripts:

∞	Free stream
$*$	Non-dimensional
$\overline{}$	Time-averaged mean value
$'$	Standard deviation
$\wedge$	Amplitude at frequency ω^*

3 Numerical method

The numerical calculations were performed with the Finite-Volume-Code FLOWer [14], provided by the Institute of Design Aerodynamics of DLR Braunschweig. It solves the three-dimensional unsteady Reynolds-averaged Navier-Stokes equations (RANS) in integral form. Turbulent flow is modelled either by the algebraic model of Baldwin and Lomax [15] with the modification according to Degani and Schiff [16] or the two-equation k-ω transport model of Wilcox [17]. The spatial discretization of the solution algorithm is characterized by a cell vertex scheme and central differences. For the damping of numerical oscillations artificial second and fourth order dissipative terms are added to the governing equations. These terms are mainly controlled by the user-defined damping coefficient $k^{(4)}$. For the time integration two different time-stepping schemes were applied: A modified "global time-stepping" scheme [18] and a "dual time-stepping" scheme based on the method of Jameson [19].

For the Euler calculations a structured elliptically smoothed O-O-grid with 81x85x137=943 245 gridnodes was generated using the parametric grid generation code MegaCADs, also provided by DLR Braunschweig. Since only symmetrical flow has been investigated just one half of the wing was discretized and analyzed (Fig. 2). The farfield boundary of the grid extends about eight wing chord lengths c in all directions and the first spacing normal to the wing is about $0.01 \cdot c$ or less. For the Navier-Stokes calculations a grid refinement near the wall has been carried out and the first spacing was diminished to $2 \cdot 10^{-6}$ wing chord lengths. The resulting Navier-Stokes grid consists of 81x101x137=1 120 797 gridnodes.

All calculations have been obtained on a VPP300 vector processor unit supported by the University of Hanover. It is equiped with four vector processor elements and a computing performance of 2.2 GigaFLOPS per element. Each calculation has required at most 800 MBytes of local active memory. For a time-accurate Navier-Stokes calculation a CPU time of approximately three and a half hours was necessary.

4 Results

4.1 Experimental and numerical validation

The numerical calculations were performed at $M_\infty = 0.2$, $Re_\infty = 1.55 \cdot 10^6$ and at angles of attack varying between $\alpha = 0°$ and $48°$. For validation the numerical solutions have been compared with experimental results measured

on the VFE configuration according to H. Oelker [20] and T. Löser [21]. In addition, grid refinement as well as variations of the artificial damping coefficient $k^{(4)}$ have been carried out in order to analyse the influence of the numerical dissipation.

4.1.1 Comparison with experiments

Fig. 3 shows the time-averaged mean value and standard deviation of the lift, drag and pitching moment coefficients, C_L, C_D and C_m. The time-averaged values of the lift coefficient C_L are calculated for a long time period $t_2 - t_1$ in the converged solution as follows:

Mean value:

$$\overline{C}_L = \frac{1}{n} \sum_{t_1}^{t_2} C_L \quad , \qquad (1)$$

Standard deviation:

$$C_L{}' = \sqrt{\frac{1}{n-1} \sum_{t_1}^{t_2} \left(C_L - \overline{C}_L \right)^2} \quad . \qquad (2)$$

n denotes the number of timesteps Δt. In the same manner the mean value and the standard deviation of the drag and pitching moment coefficients are evaluated.

In Fig. 3 the experimental data of Oelker ($M_\infty = 0.09$, $Re_\infty = 1.04 \cdot 10^6$, wing without fuselage) and Löser ($M_\infty = 0.06$, $Re_\infty = 1.55 \cdot 10^6$, wing with a half-cylinder fuselage on the bottom) are compared with the numerical Euler and Navier-Stokes computations. The higher Mach number ($M_\infty = 0.2$) in the calculations has been chosen to avoid convergence problems.

In the mean value the Euler calculations predict too high values of lift and drag and too strong nose-down pitching moments, whereas the Navier-Stokes results using the k-ω turbulence model of Wilcox agree very well with the experiments. For the VFE configuration both Löser and Oelker have observed significant changes of the flow type from a steady to an unsteady bursted vortical flow at $\alpha = 18°$ and from bursted vortical flow to deadwater-type flow at $\alpha = 43°$. These distinct angles of attack are well predicted by the Euler and the Navier-Stokes calculations. In addition, for the deadwater-type flow at $\alpha \geq 43°$ the Euler and Navier-Stokes results are identical and they are in excellent agreement with the measurements.

The fluctuations of the force and moment coefficients are zero for small angles of attack $\alpha < 18°$ and they increase for higher angles of attack. At $\alpha = 43°$ the fluctuations are strongly diminished. Although the Euler and Navier-Stokes results yield different mean values of lift, drag and pitching moment, the time-averaged fluctuations are almost the same. The increase of fluctuations at $\alpha = 18°$ and the decreasing values at $\alpha = 43°$ are also well confirmed by surface-pressure measurements according to T. Löser [21].

Fig. 4 and Fig. 5 show experimental (Löser [21]) and calculated time-averaged pressure distributions on the upper surface of the wing at a cross section $x/c = 0.6$ and for $\alpha = 21°$, $30°$, $40°$ and $45°$. The time-averaged mean value of the pressure coefficient C_p is calculated in the same manner as for the lift coefficient C_L (see eq. (1)). The y coordinate in Figs. 4 and 5 is based on the local half span s_1 depending on the streamwise position x.

For $\alpha = 21°$ the Euler result shows a typical effect: Because of the missing secondary vortex, which cannot be predicted by an Euler solver, the primary vortex is located too close to the wing and too far outwards. Therefore, the predicted suction peak in an Euler calculation is too high, thus causing a too high lift. The Navier-Stokes results, calculated with the Baldwin-Lomax (BL) and the Wilcox k-ω turbulence model, respectively, agree very well with the experiment.

At $\alpha = 21°$ the breakdown position of the primary vortex lies downstream of the analyzed cross section $x/c = 0.6$. Therefore, the primary vortex is still non-bursted for this section. For $\alpha = 30°$ and $40°$ the breakdown position has moved further upstream and the flow at $x/c = 0.6$ is dominated by a bursted primary vortex, indicated by the extremely flattened suction peaks in the time-averaged pressure distribution. For these higher angles of attack the differences between the Euler and the Navier-Stokes results decrease. Finally, at $\alpha = 45°$ with a deadwater-type flow above the wing, all numerical calculations predict the same constant suction level, which is in excellent agreement with the measurements by Löser.

After all, the time-accurate Navier-Stokes results (for both turbulence models) are well confirmed by the experiments of Oelker [20] and Löser [21] for the whole angle of attack range. On the other hand, the Euler calculated force and surface-pressure coefficients considerably deviate from the measurements. These differences decrease with higher angles of attack.

4.1.2 Influence of the artificial damping coefficient $k^{(4)}$

For angles of attack $\alpha \geq 18°$ vortex breakdown takes place and the flow above the VFE delta wing becomes unsteady. The upper part of Fig. 6 shows the lift coefficient C_L as a function of the non-dimensional time $t^* = t \cdot U_\infty/c$ at $\alpha = 20°$ for different Euler calculations with varying numerical damping coefficients $k^{(4)}$ between $1/40$ and $1/128$. After a short initial period all calculations result into converged solutions with harmonic oscillations of the lift coefficient C_L. Similar oscillations can also be observed for the drag and pitching moment coefficient C_D and C_m, respectively.

The unsteady characteristics of the harmonic lift oscillations at $\alpha = 20°$, i.e. the mean value $\overline{C}_L$, the standard deviation $C_L{}'$ and the non-dimensional period T^* are plotted against $k^{(4)}$ in the lower part of Fig. 6. Additionally, the breakdown position x_B/c is stated for $\alpha = 18°$, $19°$ and $20°$. (The criterion for the determination of the breakdown position will be presented subsequently.) For the lower angles of attack ($\alpha = 18°$ and $19°$) and high values of $k^{(4)}$ no

vortex breakdown is predicted by the Euler code and therefore, no symbols are plotted for the corresponding breakdown positions x_B/c.

The numerical dissipation $k^{(4)}$ in an Euler calculation has to simulate the missing viscous dissipation within the core of the primary vortex. Even for small values of $k^{(4)}$, it influences the strength and the size of the primary vortex and therefore the size, the position and all unsteady characteristics of the breakdown process. For a given grid, the correct amount of the artificial numerical dissipation $k^{(4)}$ in an Euler calculation has to be calibrated, e.g. with an experimentally proved breakdown position. In agreement with Oelker [20] and Löser [21], who both observed the breakdown position located at the trailing edge ($x_B/c \approx 1.0$) at $\alpha = 18°$, a value of $k^{(4)} = 1/80$ was chosen.

Fig. 7 shows the corresponding Navier-Stokes results, calculated at $\alpha = 21°$ with the Baldwin-Lomax (BL) and the Wilcox k-ω turbulence model. Since the algebraic Baldwin-Lomax model [15] provides only additional turbulent eddy viscosity within the boundary layer near the wall, the situation within the primary vortex core is still dominated by the numerical dissipation as in the case of an Euler calculation. Therefore, the numerical damping coefficient $k^{(4)}$ still has a strong effect on the breakdown process and on its position, even for small values of $k^{(4)}$. For this reason, a time-accurate Navier-Stokes code using the Baldwin-Lomax turbulence model has also to be calibrated according to experimental results. On the other hand, the two-equation k-ω model of Wilcox [17] is able to represent sufficient turbulent eddy viscosity in the primary vortex core. Therefore, all unsteady characteristics of the breakdown process, as well as the breakdown position, become independent from the numerical dissipation if the value of $k^{(4)}$ is small enough. The same effect occurs for an increasing grid resolution.

A time-accurate Navier-Stokes code with the Wilcox k-ω turbulence model is numerically validated by the present investigations, that means, it leads to the same converged solution independent from the grid resolution and from the numerical damping coefficient $k^{(4)}$. On the other hand, time-accurate Euler and Navier-Stokes codes with the Baldwin-Lomax turbulence model depend on the grid resolution and on $k^{(4)}$. For these methods the correct amount of artificial numerical dissipation $k^{(4)}$ has to be calibrated for a given grid according to experimental results.

4.2 Bursted vortical flow at $\alpha \geq 18°$

4.2.1 Spiral-type vortex breakdown

Fig. 8 shows the converged part of the lift curve C_L with respect to the non-dimensional time t^* for the Navier-Stokes calculation with the Wilcox k-ω model at $\alpha = 21°$. The artificial numerical dissipation was chosen as $k^{(4)} = 1/80$. A spectral frequency analysis of the harmonic lift oscillation $\hat{C}_L(\omega^*)$ reveals a significant reduced radian frequency

$\omega_1^* = 2\pi/T_1^* = 15.26$, corresponding to a non-dimensional period of $T_1^* = 0.41$. In the following, one period T_1^* of the lift oscillation will be analyzed in detail.

Fig. 9 shows the time-averaged mean value and standard deviation of the pressure coefficient C_p on the upper surface of the wing. In the mean value a typical pressure distribution with minimum surface pressures just beneath the primary vortex axis is predicted by the Navier-Stokes code. Between this region and the leading edge a second smaller suction peak can be observed, caused by the secondary vortex. Vortex breakdown is indicated by a significant flattening of the primary suction peak in the rear part of the wing. In this region considerable fluctuations of C_p can be observed, whereas on the rest of the wing the flow is almost steady. In the rear part two distinct centres of maximum fluctuation establish: One beneath the primary vortex (with values up to $C_p' = 0.09$) and a second one closer to the tip beneath the secondary vortex ($C_p' = 0.08$).

Fig. 10 shows lines of constant total pressure losses within a crossflow plane at $x/c = 0.95$ for the four times marked in Fig. 8. In addition, the mean value and the standard deviation of the total pressure losses, calculated for one oscillation period, are shown. For all times a main region of total pressure loss within the primary vortex can be observed. Between this main region and the wing tip a second region with increased total pressure losses can be observed, caused by the feeding sheet of the primary vortex and the counter-rotating secondary vortex, but both effects cannot be separated.

Within the primary vortex the point of maximum total pressure loss is always excentered and it rotates with respect to time in the same sense as the primary vortex is turning around. The frequency of this rotation exactly coincides with the oscillation frequency ω_1^* of the lift coefficient C_L. This behaviour leads to a very flat region of maximum total pressure loss for the mean value and to a ring-shaped region of maximum fluctuations for the standard deviation. Just beside this ring-shaped region a second region with increased fluctuations in total pressure can be observed, which belongs to the secondary vortex. This region indicates, that the secondary vortex is influenced by the bursted primary vortex and which leads to the second region of increased fluctuations of surface pressure C_p' in Fig. 9. This numerical result is in very good agreement with C. Breitsamter [22] from the Technical University of Munich. He also has measured a ring-shaped region of maximum turbulence in a plane across the bursting leading-edge vortex of a 76° swept delta wing. (These measurements were performed by hot-wire anemometry.)

Connecting the points of maximum total pressure losses for the primary and the secondary vortex at a given time t^* leads to an instantaneous primary and secondary vortex axis, respectively. In the same way the corresponding mean vortex axes can be evaluated within the time-

averaged flowfield. Fig. 11 shows these distinct axes in a perspective view above the delta wing for different times t^*. Downstream of a certain position close to the trailing edge all instantaneous primary vortex axes deviate from the mean primary vortex axis and spiral in space against the sense of the primary vortex. In addition, the instantaneous vortex axes turn around with respect to time in the sense of the primary vortex. An evaluation of the mean value of the axial velocity $\bar{u}_a$ with respect to the mean primary vortex axis indicates a reverse-flow region ($\bar{u}_a < 0$), which is surrounded by the spiraling instantaneous vortex axes (see the boundary surface with zero axial velocity $\bar{u}_a = 0$ in Fig. 11). Because of the unsteady rotation of the instantaneous primary vortex axes, the instantaneous secondary vortex axes in the rear part of the wing execute a vertical oscillation with the same reduced frequency ω_1^*.

The time-accurate Navier-Stokes code clearly predicts a spiral-type vortex breakdown of the primary vortex, which is well confirmed by experimental observations (see [1] - [5]). In addition, the predicted structure of the spiral-type vortex breakdown agrees very well with the corresponding Euler results (see J. Müller and D. Hummel [12], [13]). The only difference lies in the mutual interference of the bursted primary vortex and the secondary vortex.

The effect of the secondary vortex on the breakdown process can be seen in Fig. 12. In this figure lines of constant mean axial velocity $\bar{u}_a/U_\infty$ for a longitudinal section along the mean primary vortex axis are plotted for Euler and Navier-Stokes calculations at $\alpha = 21°$. For both methods the same damping coefficient $k^{(4)} = 1/80$ and the same grid resolution (except within the boundary layer) were chosen. In both cases a considerable change of the velocity profiles from a "jetlike" to a "wakelike" shape can be observed, finally resulting in a reverse flow. Although the structure of the velocity profiles is very similar, the Euler-predicted reverse-flow region is located further downstream in comparison with the Navier-Stokes result. This effect is caused by the missing secondary vortex in an Euler calculation, which leads to a location of the primary vortex axis closer to the wing and to a delayed upstream movement of the enlarged breakdown region across the trailing edge of the wing.

At last, Fig. 13 shows the distribution of several quantities along the mean primary vortex axes for the Euler and Navier-Stokes calculations. In both cases a sigificant increase of the mean value of the pressure coefficient $\overline{C}_p$ and a decrease of the axial velocity $\bar{u}_a/U_\infty$ can be observed, finally leading to reverse flow. In the front part of the mean vortex axes the fluctuations of total pressure $p_t{}'/p_{t\infty}$ are almost zero, and they increase very close to the starting point of the reverse-flow region with zero axial velocity ($\bar{u}_a = 0$). All these flow details are predicted very similarly by the Euler and the Navier-Stokes code. Only the streamwise positions of these distinct spatial phases within the breakdown process are different. (For further details about the

distinct phases of the breakdown process see J. Müller and D. Hummel [12]).

4.2.2   *Increasing angle of attack*

Fig. 14 shows the time-averaged mean value and standard deviation of the upper surface pressure C_p calculated by the time-accurate Navier-Stokes code with the k-ω turbulence model at $\alpha = 30°$ and $40°$. In the mean value the region of flattened primary suction peaks contineously enlarges in upstream and spanwise direction. At $\alpha = 40°$ this region almost reaches the wing apex, and the distinct suction peaks induced by primary and secondary vortex are no longer separated. Considering the standard deviation $C_p{}'$ the flow above almost the whole wing has become unsteady and the amount of the fluctuations in surface pressure grows with increasing angle of attack. Both effects, i.e. the progressive flattening of the mean suction peaks and the increasing fluctuations $C_p{}'$, indicate the contineous upstream movement of the breakdown position with increasing angle of attack.

Fig. 15 shows the distribution of several quantities along the mean primary vortex axes for increasing angle of attack. Again the strong increase of the mean pressure coefficient $\overline{C}_p$ and the decrease of the mean axial velocity $\bar{u}_a/U_\infty$ at the beginning of the breakdown process can be observed for all angles of attack. Furthermore, the strong gradients in $\overline{C}_p$ and $\bar{u}_a/U_\infty$ are almost equal for the different angles of attack. With increasing angle of attack the fluctuations in total pressure $p_t{}'/p_{t\infty}$ grow up, and the point of the "beginning unsteadiness" (with $p_t{}' > 0$) as well as the starting point of the reverse-flow region (with $\bar{u}_a = 0$) contineously move upstream. At $\alpha = 30°$ and $40°$ one large reverse-flow region establishes, covering almost the whole upper surface of the wing.

Summarizing, Fig. 16 shows the Euler and Navier-Stokes calculated breakdown positions with varying angle of attack using different criteria for determination. Because of the strong upstream effect of the breakdown process, the point of the beginning fluctuations in total pressure ($p_t{}' > 0$) moves too far upstream for high angles of attack. Therefore, the best criteria for the determination of the breakdown position are the deviation point of the instantaneous primary vortex axes and the starting point of the reverse-flow region (with $\bar{u}_a = 0$). Comparing the Euler and Navier-Stokes calculated positions using the same deviation point criterion shows very good agreement for large angles of attack $\alpha = 30°$ and $40°$. For lower angles of attack ($\alpha \leq 23°$) the Euler calculated breakdown positions are predicted too far downstream. As noted before, this effect can be explained by the missing secondary vortex in an Euler calculation, which causes a delay of the upstream movement of the breakdown region across the trailing edge of the wing. For higher angles of attack this effect diminishes. The Euler calculations were calibrated at $\alpha = 18°$ by the experimentally proved breakdown position at $x/c = 1.0$

according to H. Oelker [20] and T. Löser [21]. A once cal-
ibrated Euler code is then able to predict the correct break-
down positions for the whole angle of attack range, espe-
cially for higher angles of attack $\alpha \geq 23°$. Also the sudden
change from bursted vortical flow to deadwater-type flow
at $\alpha = 43°$, which is well confirmed by Löser [21], takes
place automatically for a once calibrated Euler code.

Finally, Fig. 17 shows the frequency spectra of the lift
oscillations $\hat{C}_L(\omega^*)$ for the Euler and Navier-Stokes calcu-
lations with the k-ω model and for different angles of at-
tack. For all spectra several strong narrow-band frequency
peaks in the lift amplitude $\hat{C}_L$ occur, which belong to sev-
eral dominating frequencies ω^*. These frequency spec-
tra for both the Euler and the Navier-Stokes calculations
are very similar to the spectra evaluated by time-accurate
surface-pressure measurements according to I. Gursul [5]
and C. Breitsamter [22]. A detailed frequency analysis re-
veals three main dominating frequencies, which belong to
three main modes of oscillation of the bursted primary vor-
tex: An azimuthal, an axial and a radial mode. These main
modes and frequencies are well confirmed by the experi-
ments of I. Gursul [5] and C. Breitsamter [22] measured
for different delta wings with varying leading edge sweep.
(For further details about these modes of oscillation see J.
Müller and D. Hummel [13]).

The highest dominating frequency ω_1^* marked in Fig.
17 belongs to the azimuthal mode of oscillation associated
with the rotation of the spiraling primary vortex axes with
respect to time (see Fig. 11). This frequency slowly de-
creases with increasing angle of attack. Based on his time-
accurate measurements C. Breitsamter [22] was able to de-
termine a correlation for this dominating frequency ω_{1e}^* de-
pending on the sweep angle of the delta wing φ and the
angle of attack α:

$$\omega_{1e}^* \cdot \cot\varphi \cdot \sin\alpha \cong 1.759 \pm 0.314 \quad . \qquad (3)$$

The corresponding curve for the $65°$ swept VFE delta wing
is also plotted in Fig. 17. For the Navier-Stokes results, the
agreement between ω_1^* and the correlation of Breitsamter
ω_{1e}^* is very good. For the Euler calculations, the azimuthal
frequency ω_1^* is slightly overpredicted for angles of attack
$\alpha \leq 23°$. This is also an effect of the missing secondary
vortex in an Euler calculation. Therefore, a time-accurate
Euler code predicts a breakdown position located too far
downstream with too high frequencies for lower angles of
attack. For higher angles of attack $\alpha > 23°$ the agreement
between the Breitsamter correlation and the Euler calcu-
lated frequencies is getting better.

4.3   Deadwater-type flow at $\alpha \geq 43°$

At $\alpha = 43°$ the breakdown position reaches the wing apex
and the vortical character of the flowfield suddenly changes

to a deadwater-type flow. For the Navier-Stokes calcula-
tion with the k-ω model, Fig. 18 shows the time-averaged
upper-surface pressures (mean value and standard devia-
tion) and time-averaged streamtraces at $\alpha = 45°$. For the
mean value of C_p an almost constant pressure distribution
on the upper surface of the wing can be observed. The
fluctuations in surface pressure are equally distributed but
rather small (see for comparison Fig. 14 at $\alpha = 40°$). On
the lower surface the time-averaged flowfield is attached,
with an attachment line A_0 parallel to the leading edge. On
the upper surface the flow is completely separated. Framed
by an attachment line A_1 near the trailing edge and a sep-
aration line S_1 along the leading edge a slow reverse flow
can be observed atop almost the whole upper surface of the
wing.

This deadwater-type flow at very high angles of at-
tack is almost equally predicted by the Euler and the
Navier-Stokes code, respectively. Fig. 19 shows the Eu-
ler and Navier-Stokes calculated time-averaged total pres-
sure losses and velocity vectors within a longitudinal sec-
tion at half wing span $y/s = 0.5$. As a reference vector the
free stream velocity U_∞ is plotted. Above the wing a large
region with almost constant total pressure losses up to 4
percent can be observed. The velocity within this region
is almost zero and the flowfield is rather unstructured. The
differences between the Euler and Navier-Stokes results are
very small.

Finally, Fig. 20 shows the standard deviation of total
pressure for the longitudinal section at $y/s = 0.5$. The fluc-
tuations of total pressure are largest at the border of the
deadwater region , whereas near the upper surface they are
almost zero. A time-accurate analysis reveals no significant
dominating frequencies, and no typical von Kármán vortex
street establishes. Again the Euler and Navier-Stokes re-
sults are very similar, although the fluctuations are a little
bit higher for the Euler calculation in comparison to the
Navier-Stokes result.

The occurrence of a deadwater-type flow at high an-
gles of attack is well confirmed by experiments (see e.g.
T. Löser [21]). For a calibrated Euler code, the numeri-
cal dissipation also simulates the necessary viscous dissipa-
tion within the separated deadwater region above the wing.
Therefore, a time-accurate Euler code is able to predict this
kind of flow correctly, if the right amount of artificial nu-
merical dissipation $k^{(4)}$ is added. This is only possible since
the separation edges for the deadwater-type flow are fixed
by the sharp edges of the VFE delta wing. This would not
be satisfied for a thick body with rounded edges.

5   Conclusions

The numerical dissipation in Euler and Navier-Stokes cal-
culations with the algebraic Baldwin-Lomax turbulence
model has to simulate the missing viscous dissipation

within the core of the primary vortex. Therefore, it influences the strength and the size of the primary vortex as well as the position and all unsteady characteristics of the breakdown process. For this reason, both methods have to be calibrated, e.g. by an experimentally proved breakdown position. On the other hand, the two-equation k-ω model of Wilcox is able to represent sufficient turbulent eddy viscosity in the primary vortex core. Therefore, a time-accurate Navier-Stokes calculation with the k-ω turbulence model becomes independent of the artificial numerical dissipation $k^{(4)}$ and the grid resolution. In addition, the agreement with experiments is very good.

Because of the missing secondary vortex in an Euler calculation, the predicted primary vortex is located too close to the wing and too far outwards. Therefore, the Euler calculated force and moment coefficients as well as the upper-surface pressure distributions differ considerably from the Navier-Stokes results and from experiments. Because of the wrong vertical position of the primary vortex relative to the wing, the upstream movement of the breakdown region across the trailing edge is delayed for angles of attack $18° \leq \alpha \leq 23°$. In addition, the highest dominating frequency ω_1^* associated to the rotating motion of the spiraling primary vortex axes is overpredicted in this angle of attack range. On the other hand, the influence of the secondary vortex on the bursted primary vortex decreases with increasing angle of attack. Therefore, the Euler predicted breakdown positions and frequencies agree very well with the Navier-Stokes results for angles of attack $\alpha > 23°$. Also the differences in surface-pressures and force coefficients diminish with increasing angle of attack. Finally, at very high angles of attack $\alpha \geq 43°$ with a deadwater-type flow above the wing, the Euler and Navier-Stokes results with k-ω turbulence model are almost identical. However, a time-accurate Euler calculation needs only two thirds of the computation time necessary for a Navier-Stokes calculation.

6 Final remarks

It is gratefully acknowledged, that the Institute of Design Aerodynamics of the DLR Braunschweig provided the Finite-Volume-Code FLOWer as well as the grid generation program MegaCADs.

7 References

[1] Lambourne N and Bryer D. The bursting of leading-edge vortices. *ARC R. & M.*, No. 3282, 1962.

[2] Hummel D and Srinivasan P. Vortex breakdown effects on the low speed aerodynamic characteristics of slender delta wings in symmetrical flow. *Journal Roy. Aeron. Soc.*, Vol. 71, pp 319-322, 1967.

[3] Hummel D. On the vortex formation over a slender delta wing at large angles of incidence. *AGARD-CP*, No. 247, pp 15-1 to 15-7, 1978.

[4] Nelson R and Visser K. Breaking down the delta wing vortex – The role of vorticity in the breakdown process. *AGARD-CP*, No. 494, pp 21-1 to 21-15, 1990.

[5] Gursul I. Unsteady flow phenomena over delta wings at high angle of attack. *AIAA Journal*, Vol. 32, pp 225-231, 1994.

[6] Rizzi A, Erikson L, Schmidt W and Hitzel S. Simulating vortex flows around wings. *AGARD-CP*, No. 342, pp 21-1 to 21-14, 1983.

[7] Ekaterinaris J and Schiff L. Vortical flows over delta wings and numerical prediction of vortex breakdown. *AIAA Paper*, No. 90-0102, 1990.

[8] Visbal M. Structure of vortex breakdown on a pitching delta wing. *AIAA Paper*, No. 93-0434, 1993.

[9] Longo J. Compressible inviscid vortex flow of a sharp edged delta wing. *AIAA Journal*, Vol. 33, No. 4, pp 680-686, 1995.

[10] Strohmeyer D, Orlowski M, Longo J, Hummel D and Bergmann A. An analysis of vortex breakdown predicted by the Euler equations. *Proc. 20th ICAS Congress*, Sorento, Vol. 1, pp 1189-1200, 1996.

[11] Drougge G. The international vortex flow experiment for computer code validation. *Proc. 16th ICAS Congress*, Jerusalem, Vol. 1, pp XXXV-XLI, 1988.

[12] Müller J and Hummel D. An analysis of vortex breakdown predicted by a time-accurate Euler code. *Notes on Numerical Fluid Mechanics*, Vol. 72, pp 331-338, 1999.

[13] Müller J and Hummel D. Time-accurate CFD analysis of the unsteady flow on a fixed delta wing. *AIAA Paper*, No. 2000-0138, 2000.

[14] Aumann P, Bartelheimer W, Bleecke H, Eisfeld B, Lieser J, Heinrich R, Kroll N, Kuntz M, Monsen E, Raddatz J, Reisch U and Roll B. *FLOWer: Installation and User Handbook*, Release 115, DLR Braunschweig, 1998.

[15] Baldwin B and Lomax H. Thin layer approximation and algebraic model for separated turbulent flows. *AIAA Paper*, No. 78-257, 1978.

[16] Degani D and Schiff L. Computation of turbulent supersonic flows around pointed bodies having crossflow separation. *Journal Comp. Physics*, Vol. 66, pp 173-196, 1986.

[17] Wilcox D. *Turbulence modeling for CFD*, 2nd edition, DCW Industries Inc., 1998.

[18] Pahlke K. Development of a numerical method solving the unsteady Euler equations for airfoils and arbitary motions. *DLR-IB*, No. 129-92-09, 1992.

[19] Jameson A. Time dependent calculations using multigrid with applications to unsteady flows past airfoils and wings. *AIAA Paper*, No. 91-1596, 1991.

[20] Oelker H. Aerodynamische Untersuchungen an kurzgekoppelten Entenkonfigurationen bei symmetrischer Anströmung. *Diss. TU Braunschweig*, ZLR-FB 90-01, 1990.

[21] Hummel D and Löser T. Low speed wind tunnel experiments on a delta wing oscillating in pitch. *Proc. 21st ICAS Congress*, Melbourne, No. ICAS-98-3,9,3, 1998.

[22] Breitsamter C. Turbulente Strömungsstrukturen an Flugzeugkonfigurationen mit Vorderkantenwirbeln. *Diss. TU München*, Herbert Utz Verlag Wiss., 1997.

8 Figures

Top view:
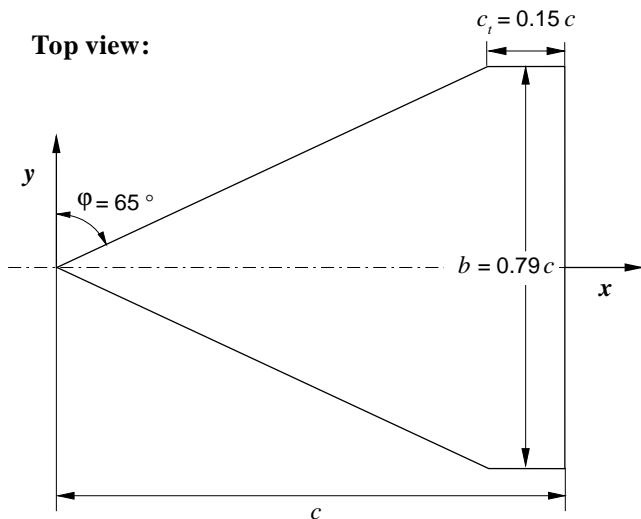
Root airfoil:
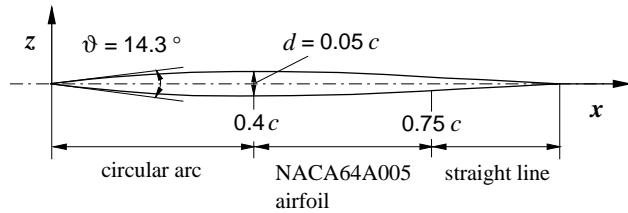
Fig. 1 : Geometry of the VFE delta wing
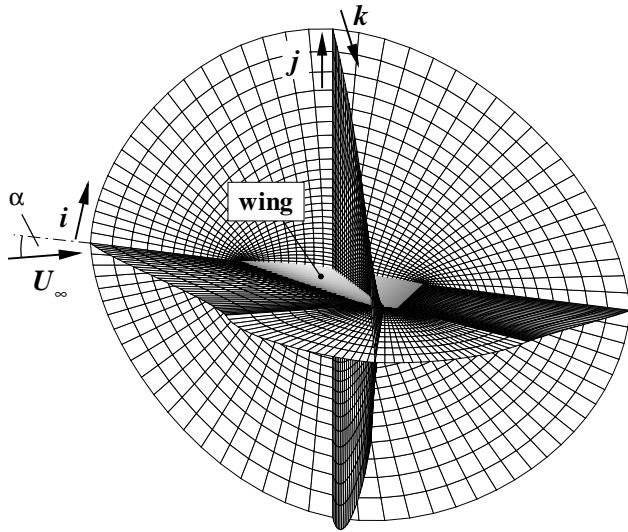
Fig. 2 : Grid section of the O-O-grid topology
with 943 245 gridnodes (Euler) and
with 1 120 797 gridnodes (Navier-Stokes)
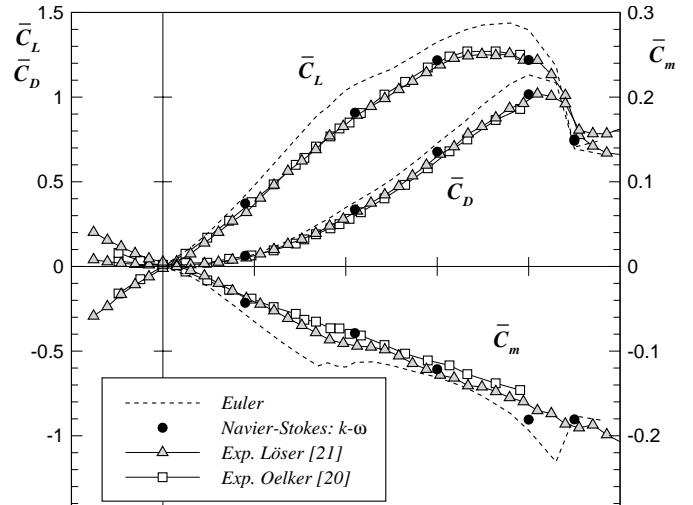
Fig. 3 : Force and moment coefficients (mean value
and standard deviation) for varying angle of
attack α ($M_\infty = 0.2$, $Re_\infty = 1.55 \cdot 10^6$)
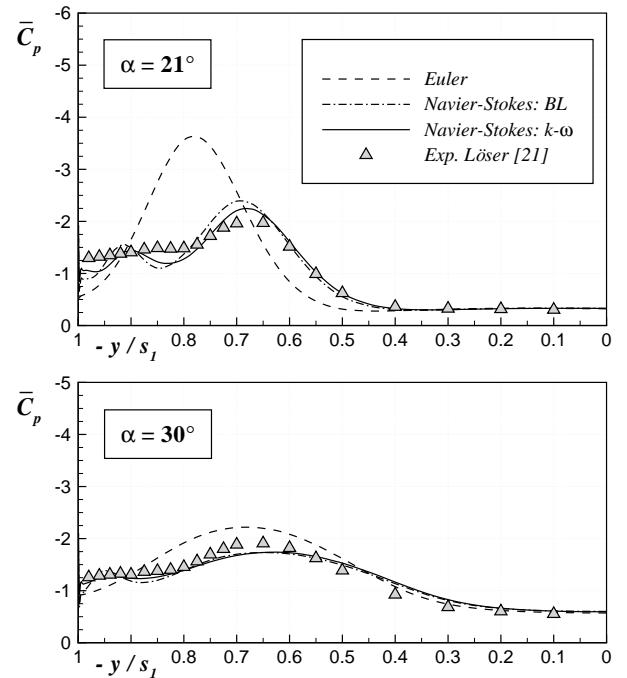
Fig. 4 : Time-averaged upper-surface pressures
at $x/c = 0.6$, $\alpha = 21°$ and $30°$
($M_\infty = 0.2$, $Re_\infty = 1.55 \cdot 10^6$)
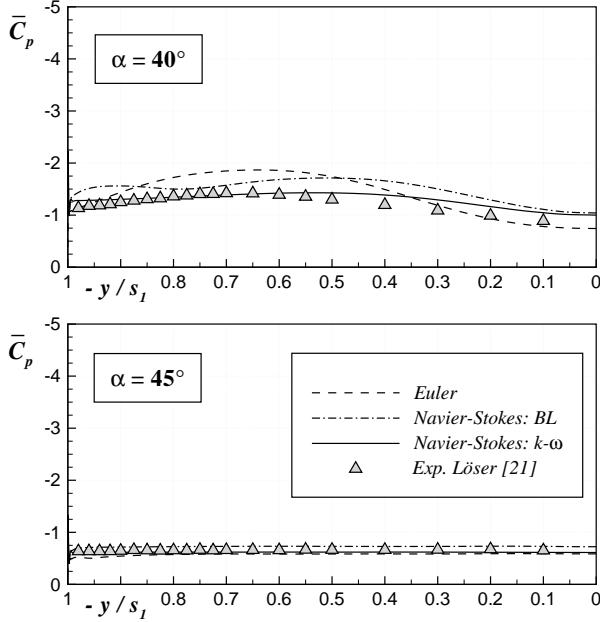
Fig. 5 : Time-averaged upper-surface pressures
at $x/c = 0.6$, $\alpha = 40°$ and $45°$
($M_\infty = 0.2$, $Re_\infty = 1.55 \cdot 10^6$)
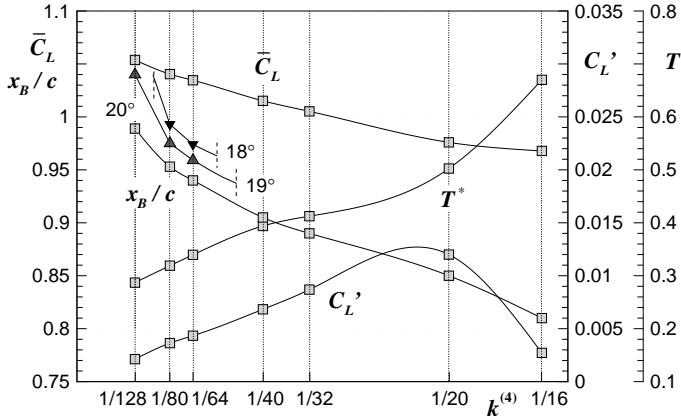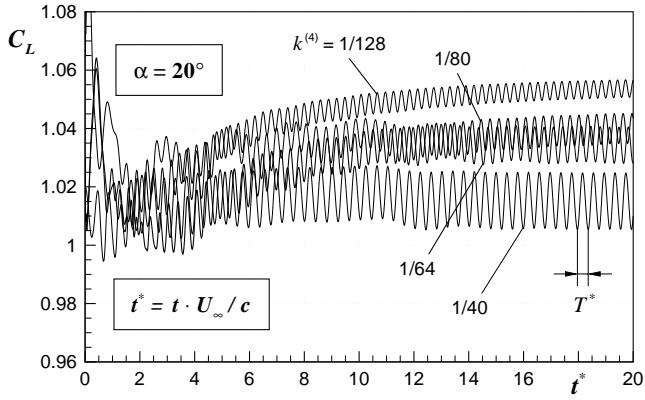
Fig. 6 : Influence of $k^{(4)}$ on the lift curve $C_L(t^*)$, the unsteady characteristics $\overline{C}_L$, C_L', T^* and the breakdown position x_B/c (Euler: $\alpha = 20°$)
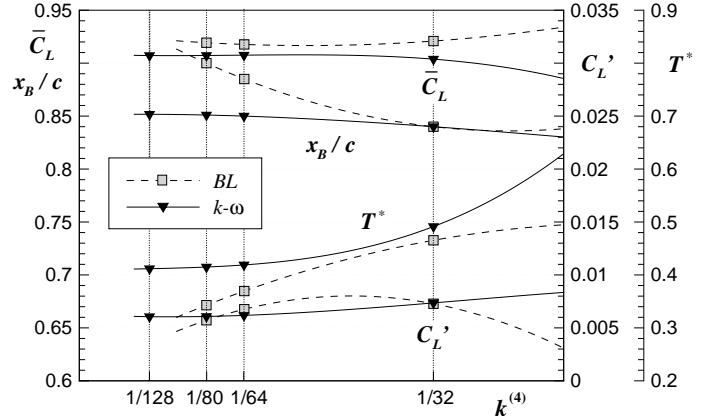
Fig. 7 : Influence of $k^{(4)}$ on the unsteady characteristics $\overline{C}_L$, C_L' and T^* and the breakdown position x_B/c (Navier-Stokes: $\alpha = 21°$)
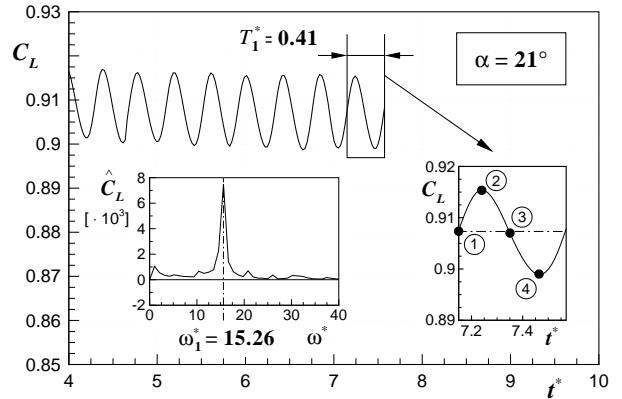
Fig. 8 : Lift curve and frequency spectrum
(Navier-Stokes (k-ω): $\alpha = 21°$)
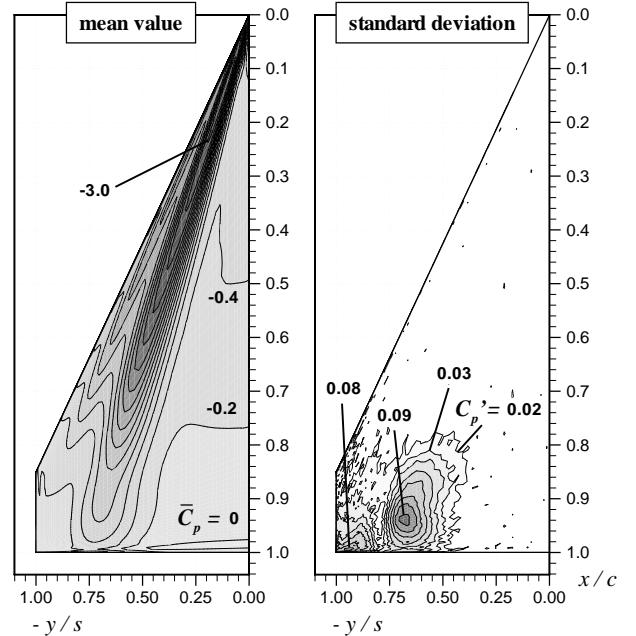
Fig. 9 : Upper-surface pressure distribution
(Navier-Stokes (k-ω): $\alpha = 21°$)
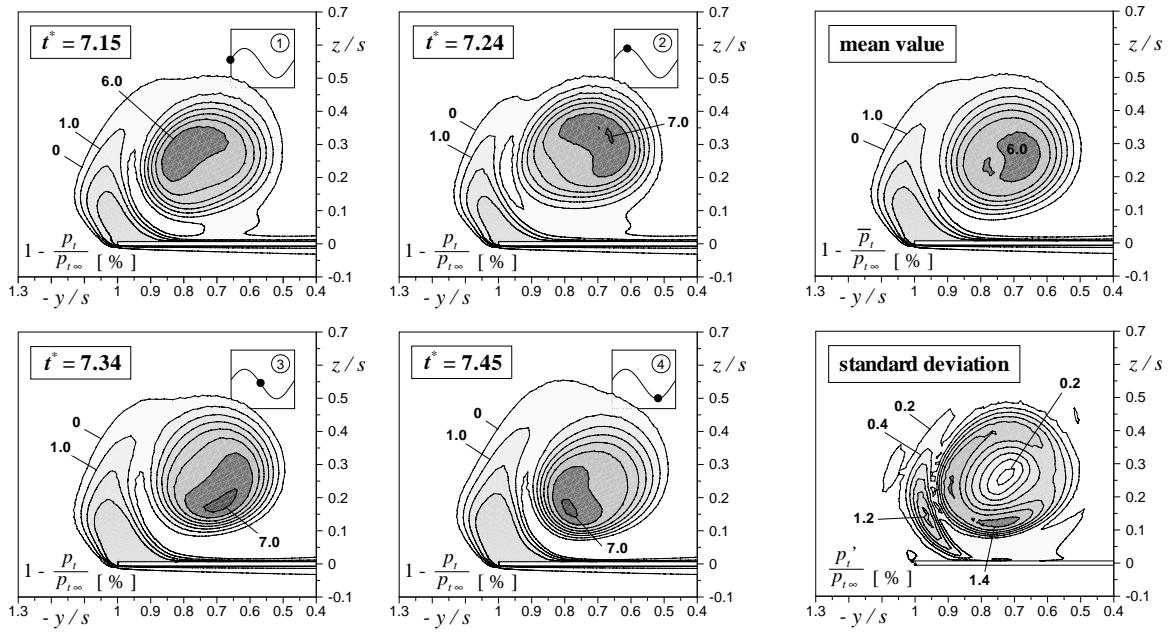
Fig. 10 : Lines of constant total pressure losses at $x/c = 0.95$ (Navier-Stokes (k-ω): $\alpha = 21°$)
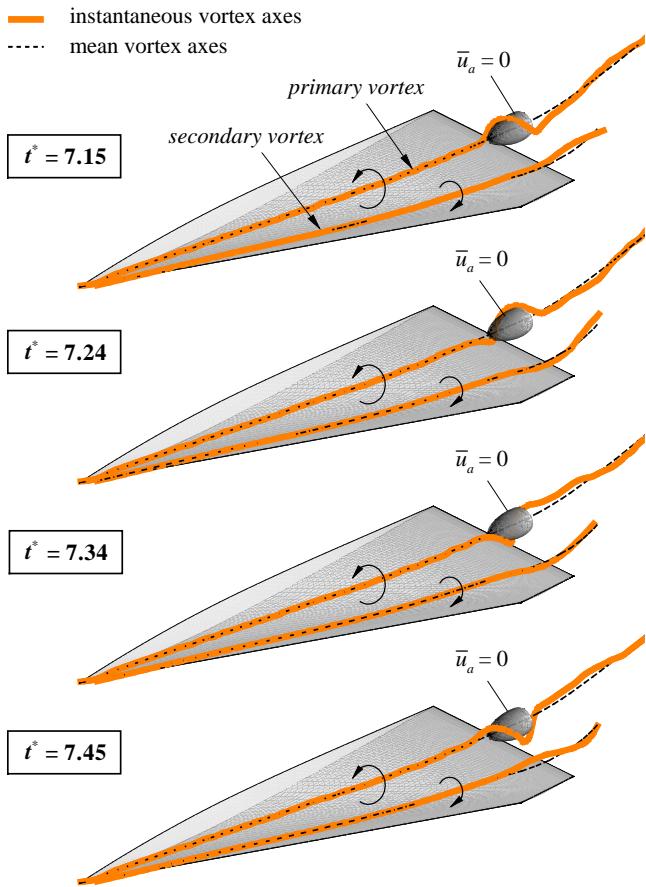
Fig. 11 : Instantaneous and mean vortex axes for different times t^* (Navier-Stokes (k-ω): $\alpha = 21°$)
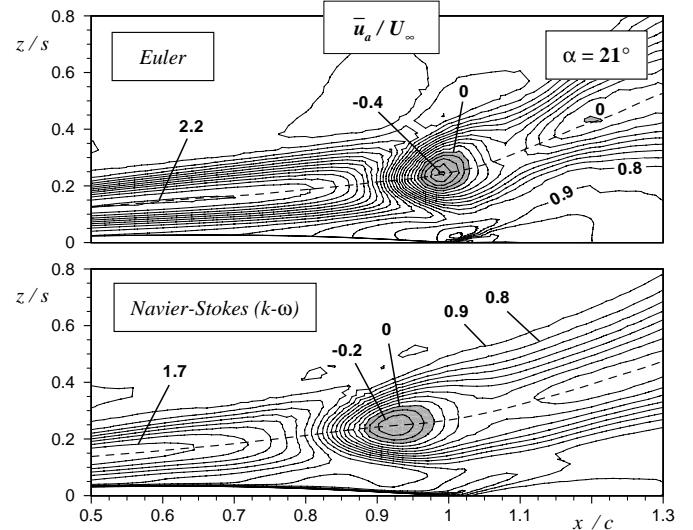
Fig. 12 : Mean axial velocity $\bar{u}_a/U_\infty$ for a longitudinal section through the mean vortex axis (Euler / Navier-Stokes (k-ω): $\alpha = 21°$)
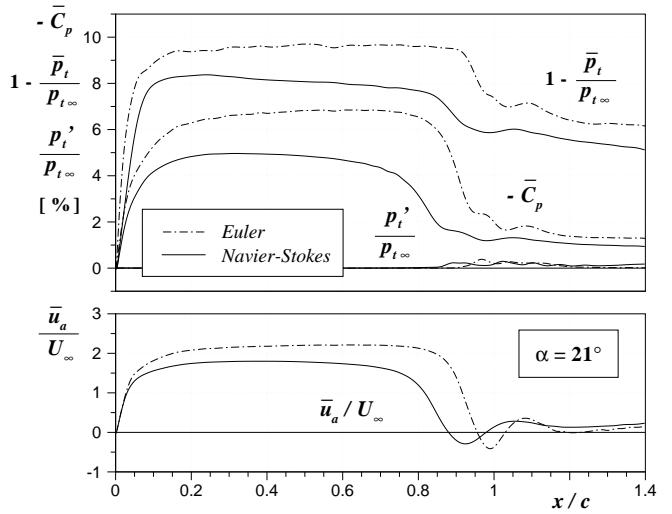
Fig. 13 : Distributions along the mean vortex axis (Euler / Navier-Stokes (k-ω): $\alpha = 21°$)
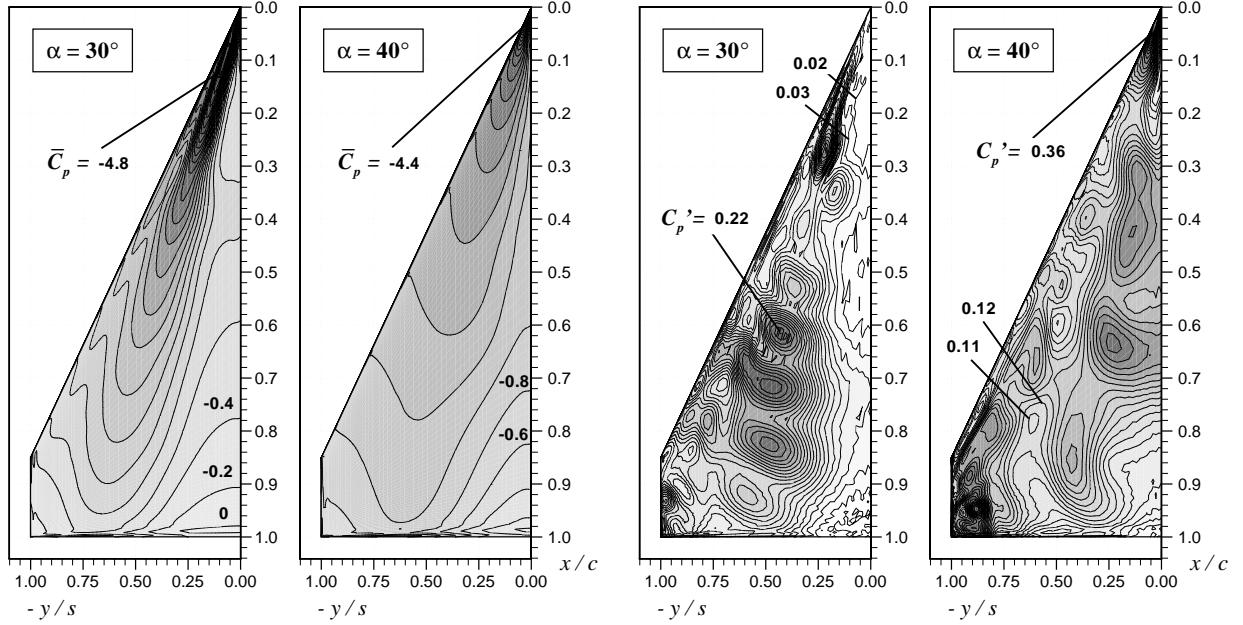
Fig. 14 : Upper-surface pressures (mean value and standard deviation) at $\alpha = 30°$ and $40°$ (Navier-Stokes (k-ω))
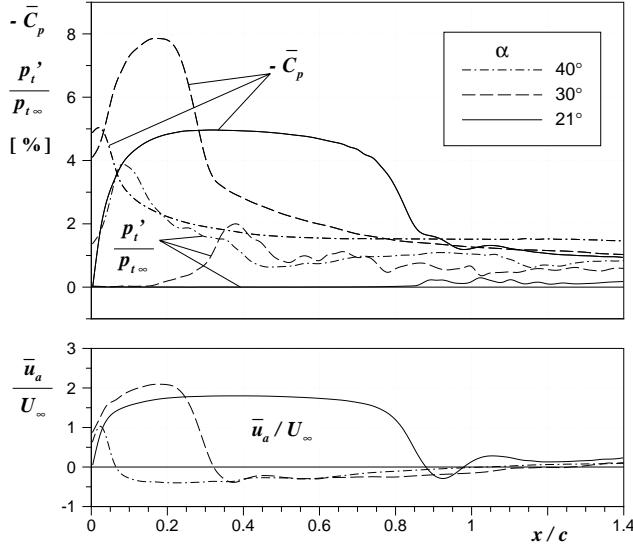
Fig. 15 : Distributions along the mean vortex axis for different angles of attack (Navier-Stokes (k-ω))
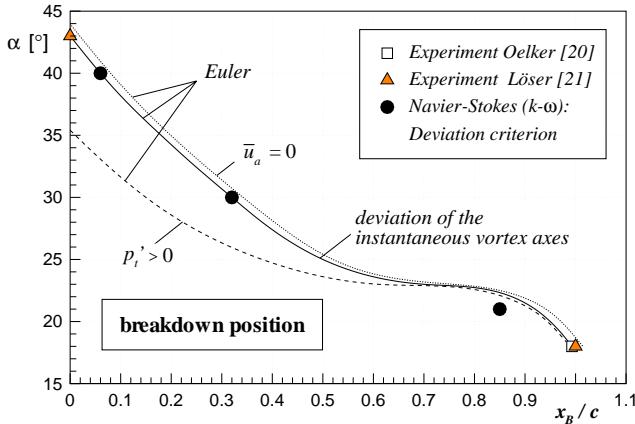

Fig. 16 : Breakdown positions for various angles of attack according to different criteria (Euler / Navier-Stokes (k-ω))
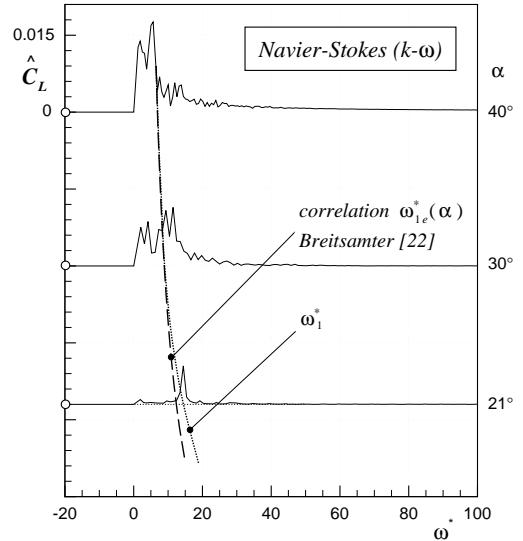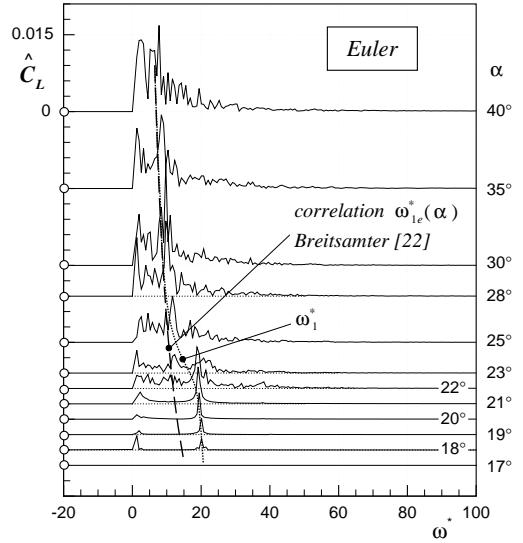

Fig. 17 : Spectral analysis of the lift oscillations for different angles of attack (Euler / Navier-Stokes (k-ω))
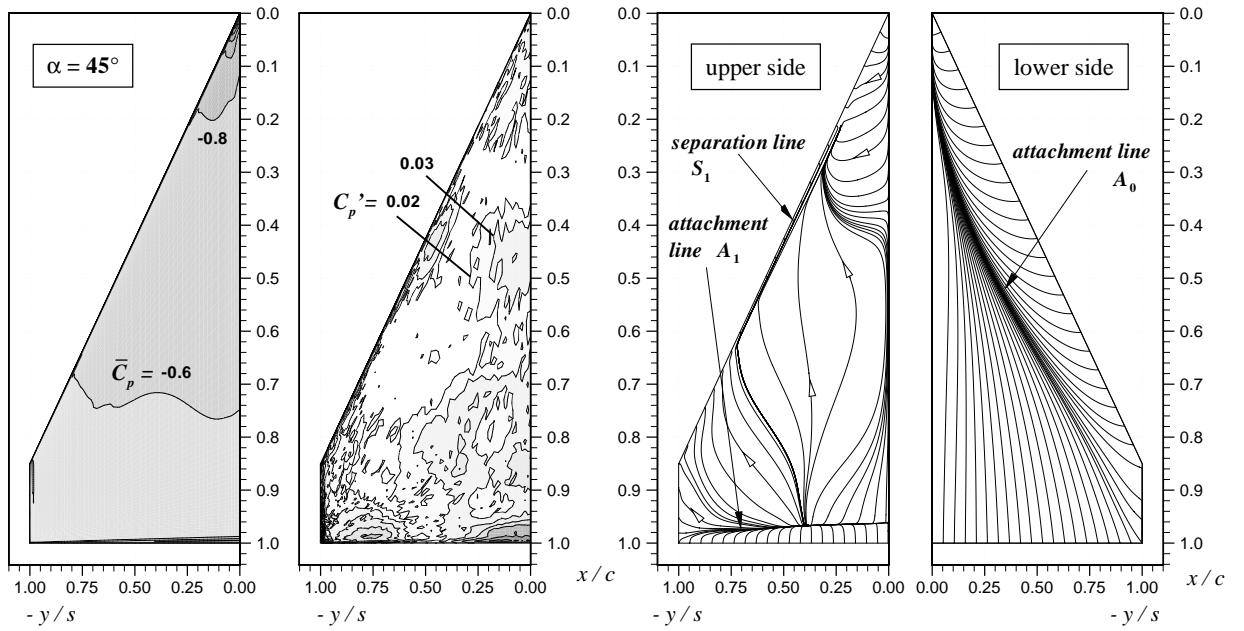
Fig. 18 : Upper-surface pressures (mean value and standard deviation) and time-averaged streamtraces
(Navier-Stokes (k-ω): $\alpha = 45°$)
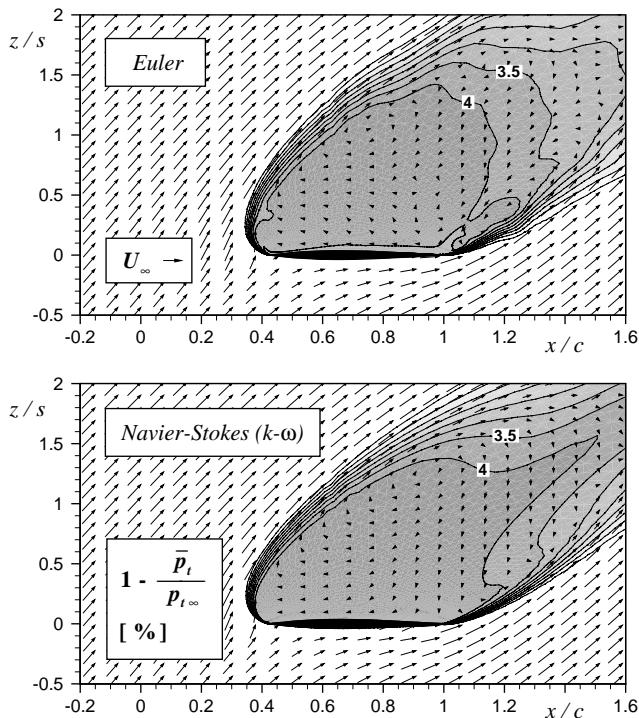
Fig. 19 : Time-averaged total pressure losses and
velocity vectors at $y/s = 0.5$
(Euler / Navier-Stokes (k-ω): $\alpha = 45°$)
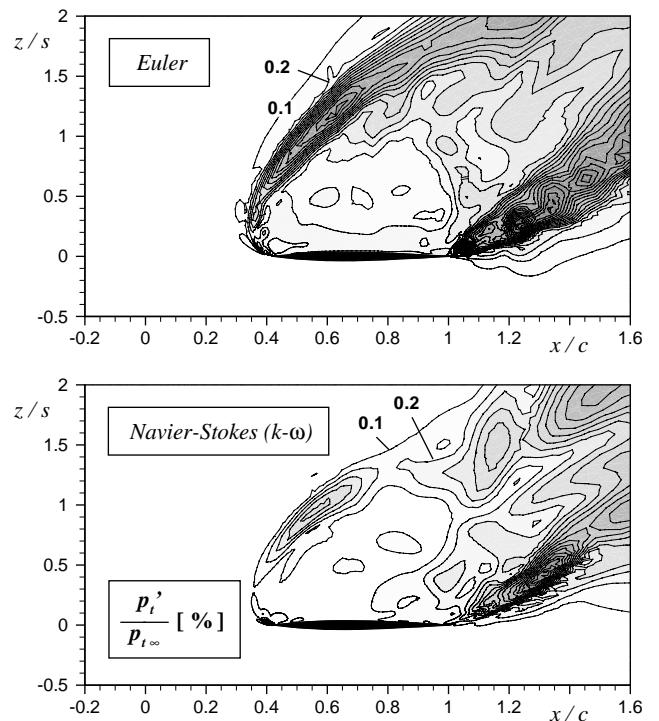
Fig. 20 : Fluctuations of total pressure at $y/s = 0.5$
(Euler / Navier-Stokes (k-ω): $\alpha = 45°$)